ARTICLE

Open Access

Lanthanide-doped heterostructured nanocomposites toward advanced optical anti-counterfeiting and information storage

Yao Xie[1,2], Yapai Song[3,4], Guotao Sun[3,4], Pengfei Hu[5], Artur Bednarkiewicz [6] and Lining Sun [2,3,4✉]

Abstract

The continuously growing importance of information storage, transmission, and authentication impose many new demands and challenges for modern nano-photonic materials and information storage technologies, both in security and storage capacity. Recently, luminescent lanthanide-doped nanomaterials have drawn much attention in this field because of their photostability, multimodal/multicolor/narrowband emissions, and long luminescence lifetime. Here, we report a multimodal nanocomposite composed of lanthanide-doped upconverting nanoparticle and EuSe semiconductor, which was constructed by utilizing a cation exchange strategy. The nanocomposite can emit blue and white light under 365 and 394 nm excitation, respectively. Meanwhile, the nanocomposites show different colors under 980 nm laser excitation when the content of Tb^{3+} ions is changed in the upconversion nanoparticles. Moreover, the time-gating technology is used to filter the upconversion emission of a long lifetime from Tb^{3+} or Eu^{3+}, and the possibilities for modulating the emission color of the nanocomposites are further expanded. Based on the advantage of multiple tunable luminescence, the nanocomposites are designed as optical modules to load optical information. This work enables multi-dimensional storage of information and provides new insights into the design and fabrication of next-generation storage materials.

Introduction

Currently, human society has entered the information age, in which our daily lives are being inundated by a huge amount of data. Recently years, researchers have focused on exploring innovative information storage devices and information storage strategies. Compared to the traditional magnetic storage and semiconductor memory, optical information storage exhibits the advantages of higher efficiency, lower energy consumption, longer storage life, and larger capacity, and thus it is widely considered as an important storage strategy for the next generation[1,2].

To date, several kinds of luminescent materials, including metallic nanocrystals[3,4], semiconductor quantum dots[5–8], metal-organic frameworks[9–13], organic dye molecules[14,15], and lanthanide-doped nanomaterials[16–23] have been developed as optical information storage media. Among them, lanthanide-doped nanomaterials have been considered as potential candidates because of their unique advantages of color-tunable luminescence[24,25], long luminescence lifetime[26,27], narrowband emission, and outstanding photochemical stability[28–30]. Due to the inherent $4f^n$ orbital and rich energy-level structures of lanthanide element, the lanthanide-doped nanomaterials exhibit excellent luminescent performance and efficient spectral conversion ability through down-shifting and upconverting processes[31]. They can emit polychromatic radiation covering the entire visible and near-infrared (NIR) spectral region when irradiated by NIR, visible, or ultraviolet (UV) light. However, the traditional single-model luminescent materials used for optical information storage have shortcomings such as small information storage capacity, which

Correspondence: Lining Sun (lnsun@shu.edu.cn)
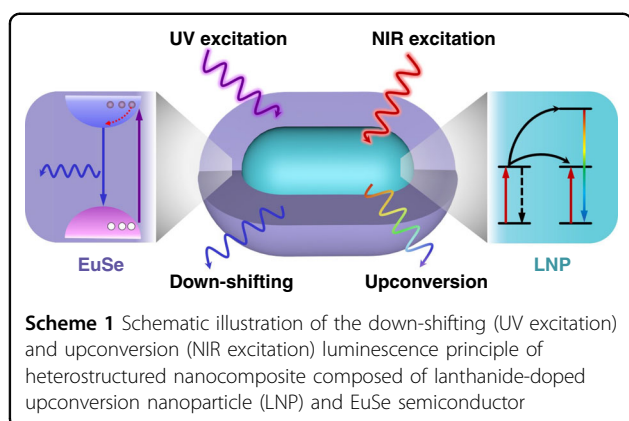[1]Department of Physics, College of Sciences, Shanghai University, Shanghai 200444, China
[2]Department of Chemistry, College of Sciences, Shanghai University, Shanghai 200444, China
Full list of author information is available at the end of the article

Scheme 1 Schematic illustration of the down-shifting (UV excitation) and upconversion (NIR excitation) luminescence principle of heterostructured nanocomposite composed of lanthanide-doped upconversion nanoparticle (LNP) and EuSe semiconductor

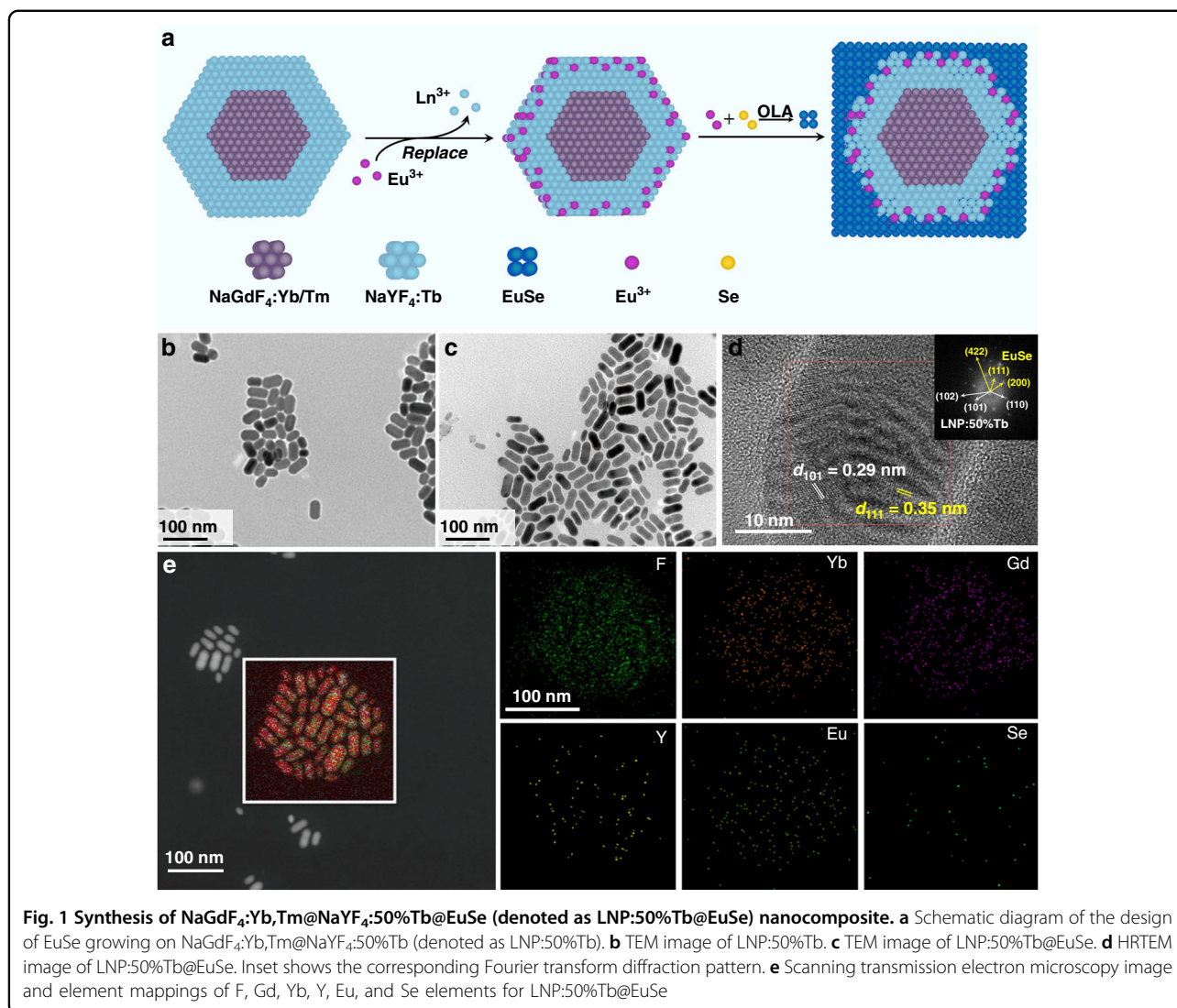drives the urgent need to develop advanced luminescent materials as information carriers.

By integrating the stokes and anti-stokes processes into the same information carriers, the multimodal emission with adjustable colors could be achieved under the different excitation wavelength, which can increase the information storage capacity of luminescent materials. Therefore, the multi-mode luminescent materials are very promising in the field of information storage because of the characteristics of information storage capacity and security. In the previous research of dual-mode luminescent materials, a variety of lanthanide elements with upconversion and down-shifting luminescent properties are often doped in the same matrix[32–34]. This strategy caused the cross-relaxation between the lanthanides, which resulted in the decrease of luminescent intensity. We would like to combine Stokes and anti-Stokes features into one system. For the former, the semiconductors are efficient. For the latter, there are no better candidate than lanthanide-doped upconversion nanoparticles. However, the epitaxial growth is difficult between semiconductors and upconversion nanoparticles. Thus, it is promising to develop innovative heterostructured multi-mode luminescent materials with intentionally designed color or well-defined tunable properties for optical information storage.

Herein, we develop a heterostructured, colloidal nanocomposite made of EuSe semiconductor and lanthanide-doped upconversion nanoparticle by utilizing a cation exchange strategy, which possess outstanding down-shifting and upconversion performances. Benefit from cation exchange strategy, the transition layer containing Eu^{3+} ions forms between the EuSe semiconductor and the lanthanide-doped upconversion nanoparticle, and the characteristic emission of Eu^{3+} ions can be detected under both UV and NIR light irradiation. As presented in Scheme 1, the nanocomposite could emit blue and white light under excitation of UV light, and also shows color modulation upconverting emission under excitation of

980 nm laser *via* controlling the type and content of lanthanide elements in the upconversion nanoparticles. In addition, the upconverting emission with a long lifetime from specific lanthanide ions could be filtered through time-gating technology. Stemming from the multimode luminescent properties of nanocomposites, we demonstrate their suitability for advanced anti-counterfeiting and information storage successfully.

Results and discussions

We developed a methodology for combining EuSe semiconductors with upconversion nanoparticles by ions exchange between different lanthanide ions. Namely, the Tb^{3+} doped $NaYF_4$ shell was homogeneously deposited on the $NaGdF_4$:49%Yb,1%Tm upconverting core (denoted as $NaGdF_4$:Yb,Tm), and in the critical step of our method the partial lanthanide ions (Tb^{3+}, Y^{3+}) on the surface of such $NaGdF_4$:Yb,Tm@$NaYF_4$:50%Tb nanoparticles were replaced by Eu^{3+} through cation exchange in the dispersion (Fig. 1a). After that, the oleylamine would be used as a reducing agent during the synthesis of EuSe, and the Eu^{3+} ions on the surface were partially reduced to Eu^{2+} ions which form the EuSe together with selenium powder[35–37]. It is generally considered that epitaxial growth is difficult when the lattice mismatch is large between two materials. In this case, the cation exchange of Eu^{3+} ions and other lanthanides could promote the formation of buffer layers to reduce the lattice mismatch and promote the heterogeneous epitaxial growth of EuSe[38,39]. As demonstrated by transition electron microscopy (TEM) images, the obtained $NaGdF_4$:Yb,Tm cores show uniform spherical morphology (Fig. S1). The lanthanide-doped upconversion nanoparticle $NaGdF_4$:Yb,Tm@$NaYF_4$:50% Tb (denoted as LNP:50%Tb) and $NaGdF_4$:Yb, Tm@$NaYF_4$:50%Tb@EuSe (LNP:50%Tb@EuSe) nanocomposite display uniform rod-like morphology and monodispersed particle (Fig. 1b, 1c). The size distributions of LNP:50%Tb and LNP:50%Tb@EuSe were measured from different directions. As shown in Fig. S2, the length of LNP:50%Tb@EuSe nanocomposite (around 44.7 nm) is significantly longer than that of LNP:50%Tb (around 35.8 nm) after growth of EuSe. Meanwhile, the X-ray diffraction patterns of the LNP:50%Tb and LNP:50%Tb@EuSe nanocomposite, as illustrated in Fig. S3, show that the intensity of diffraction peaks attributed to LNP:50%Tb is significantly lower for the nanocomposite and a broad diffraction peak appears around 25 degree. The nanocomposite exhibits low crystallinity because of the formation of buffer layers during the epitaxial growth of EuSe[39,40]. The high-resolution TEM (HRTEM) image of LNP:50%Tb@EuSe nanoparticle was shown in Fig. 1d. The lattice fringes could be well resolved and a *d*-spacing of 0.29 nm can be observed, which is attributed to the (101) plane of hexagonal $NaYF_4$. An

Fig. 1 Synthesis of NaGdF$_4$:Yb,Tm@NaYF$_4$:50%Tb@EuSe (denoted as LNP:50%Tb@EuSe) nanocomposite. a Schematic diagram of the design of EuSe growing on NaGdF$_4$:Yb,Tm@NaYF$_4$:50%Tb (denoted as LNP:50%Tb). **b** TEM image of LNP:50%Tb. **c** TEM image of LNP:50%Tb@EuSe. **d** HRTEM image of LNP:50%Tb@EuSe. Inset shows the corresponding Fourier transform diffraction pattern. **e** Scanning transmission electron microscopy image and element mappings of F, Gd, Yb, Y, Eu, and Se elements for LNP:50%Tb@EuSe

additional *d*-spacing of 0.35 nm is attributed to the (111) plane of cubic EuSe. The inset of Fig. 1d reveals that the LNP:50%Tb@EuSe is a polycrystalline nanoparticle compounded by hexagonal phase NaYF$_4$ and cubic phase EuSe.

It was reported that the lattice mismatch may lead to anisotropic shell growth and shape distortion[41,42]. In order to prove that the growth of EuSe on the surface of lanthanide-doped nanoparticles is anisotropic, we synthesized the spherical nanoparticles (NaYF$_4$:20%Yb,0.5% Tm) with homogenous morphology as a matrix, and then EuSe grew on the surface. The changes in the morphology of nanoparticles during the growth of EuSe are investigated by TEM measurement of the samples collected after heat treatment at 290 °C for different duration (0 h, 1 h, 2 h, and 3 h, respectively). As shown in Fig. S4, the morphology of nanoparticles gradually transforms from spherical to rod-like with the increase of heat treatment
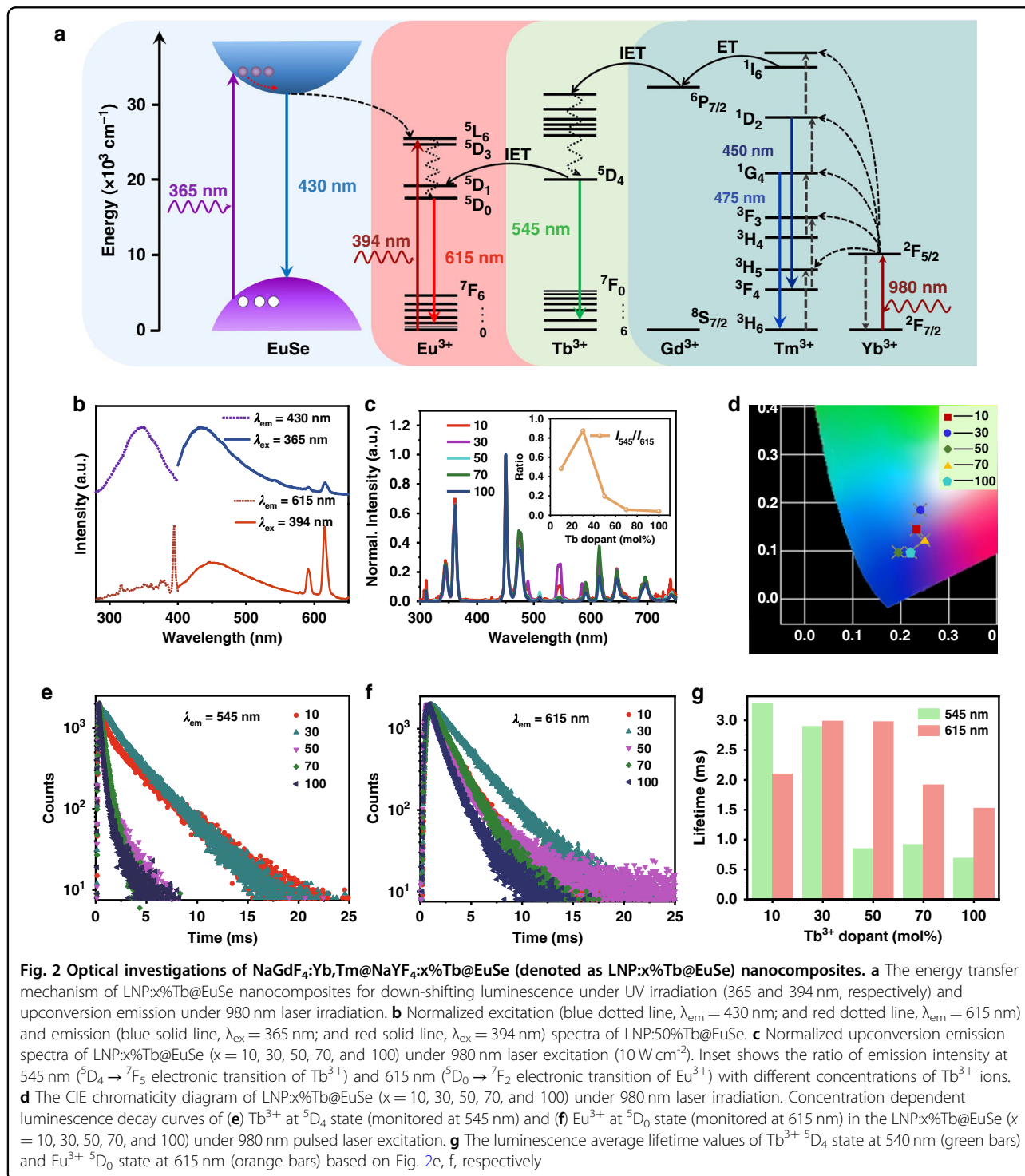
time. This indicates that the growth of cubic EuSe on the surface of hexagonal upconversion nanoparticles is anisotropic.

The growth of EuSe leads to significant changes of ligands on the nanoparticle surface (Fig. S5). Only oleic acid groups are present on the surface of LNP:50%Tb, while oleic acid and oleylamine groups coexist on the surface of LNP:50%Tb@EuSe due to the successful growth of EuSe. At the same time, compared to LNP:50% Tb, the LNP:50%Tb@EuSe nanocomposite exhibits stronger absorption in the UV region (Fig. S6). These results further demonstrate the successful growth of EuSe on the surface of LNP:50%Tb. In addition, the energy dispersive X-ray spectroscopy (EDS) and element mappings of the nanocomposites verify the distribution of F, Yb, Gd, Y, Eu, and Se over the randomly selected region (Fig. 1e and Fig. S7). It can be observed that the content of Eu element in the nanocomposite is obviously more than

that of Se element. This is due to the presence of partially unreduced trivalent europium ions in the LNP:50%Tb (see Fig. 1). The X-ray photoelectron spectroscopy (XPS) spectrum of the nanocomposite as well as high-resolution XPS spectrum at Eu 3d position of nanocomposite are shown in Fig. S8. The signals of Eu^{2+} $3d_{5/2}$, Eu^{3+} $3d_{5/2}$, Eu^{2+} $3d_{3/2}$ and Eu^{3+} $3d_{3/2}$ can be observed clearly, which

illustrates that both Eu^{2+} and Eu^{3+} ions are coexistent in these nanocomposites.

Because of the successful growth of EuSe on the surface of LNP:50%Tb, the nanocomposite can display different colors under different excitation wavelengths of UV light (Fig. 2a and b). Figure 2a displays a model that illustrates the energy transfer processes of Eu^{2+} to Eu^{3+} and the

Fig. 2 Optical investigations of NaGdF$_4$:Yb,Tm@NaYF$_4$:x%Tb@EuSe (denoted as LNP:x%Tb@EuSe) nanocomposites. a The energy transfer mechanism of LNP:x%Tb@EuSe nanocomposites for down-shifting luminescence under UV irradiation (365 and 394 nm, respectively) and upconversion emission under 980 nm laser irradiation. **b** Normalized excitation (blue dotted line, $\lambda_{em} = 430$ nm; and red dotted line, $\lambda_{em} = 615$ nm) and emission (blue solid line, $\lambda_{ex} = 365$ nm; and red solid line, $\lambda_{ex} = 394$ nm) spectra of LNP:50%Tb@EuSe. **c** Normalized upconversion emission spectra of LNP:x%Tb@EuSe (x = 10, 30, 50, 70, and 100) under 980 nm laser excitation (10 W cm^{-2}). Inset shows the ratio of emission intensity at 545 nm ($^5D_4 \rightarrow {}^7F_5$ electronic transition of Tb^{3+}) and 615 nm ($^5D_0 \rightarrow {}^7F_2$ electronic transition of Eu^{3+}) with different concentrations of Tb^{3+} ions. **d** The CIE chromaticity diagram of LNP:x%Tb@EuSe (x = 10, 30, 50, 70, and 100) under 980 nm laser irradiation. Concentration dependent luminescence decay curves of (**e**) Tb^{3+} at $^5D_4$ state (monitored at 545 nm) and (**f**) Eu^{3+} at $^5D_0$ state (monitored at 615 nm) in the LNP:x%Tb@EuSe (x = 10, 30, 50, 70, and 100) under 980 nm pulsed laser excitation. **g** The luminescence average lifetime values of Tb^{3+} $^5D_4$ state at 540 nm (green bars) and Eu^{3+} $^5D_0$ state at 615 nm (orange bars) based on Fig. 2e, f, respectively

characteristic f–f transition emission of Eu^{3+} in the nanocomposite. The emission of Eu^{2+} and Eu^{3+} will be competing under UV light irradiation when Eu^{2+} and Eu^{3+} coexist in the nanocomposites[43,44]. As presented in Fig. 2b, the excitation spectrum displays a broadband peak with a maximum at 340 nm by monitoring the emission at 430 nm, which comes from the $4f^7 \rightarrow 4f^6 5d^1$ electronic transition of Eu^{2+}. However, a sharp excitation peak at 394 nm is observed by monitoring the characteristic emission of Eu^{3+} ion at 615 nm, which is derived from the $^7F_0 \rightarrow {}^5L_6$ transition of Eu^{3+}. As shown in the emission spectrum under excitation with 365 nm, a strong broadband emission peak at 430 nm from Eu^{2+} dominates over a weak emission peak at 615 nm from $^5D_0 \rightarrow {}^7F_2$ of Eu^{3+} can be observed. Inversely, under 394 nm excitation, which is well suited for the f–f transition in Eu^{3+}, the narrowband $^5D_0 \rightarrow {}^7F_J$ Eu^{3+} emission dominate the Eu^{2+} broadband emission at 450 nm. The color coordinate values of LNP:50%Tb@EuSe nanocomposite under different wavelengths of UV excitation were plotted in the Commission Internationale de l'Eclairage (CIE) chromaticity diagram. As illustrated in Fig. S9, the color coordinate is in the blue region under 365 nm excitation, while it shifts to around white region under 394 nm excitation.

In addition, due to the energy transfer between Tb^{3+} and Eu^{3+} ions, we could change the type and content of Tb^{3+} ions in this system to control the luminescence of nanocomposites under 980 nm laser excitation[45,46]. In order to obtain multi-colored upconversion emission, we exploited the $NaGdF_4$:Yb,Tm@$NaYF_4$:x%Tb nanoparticles with different Tb content (LNP:x%Tb; $x = 10, 30, 70, and 100$, respectively) as a matrix to deposit EuSe aiming to design new multi-functional nanocomposites. The TEM images of these nanocomposites are shown in Fig. S10 and the down-shifting emission spectra in Fig. S11 (denoted as LNP:x%Tb@EuSe) demonstrate that the LNP:x%Tb are successfully coated by EuSe. Figure 2a also illustrates that an energy transfer pathway is successfully constructed by the introduction of Yb^{3+}, Tm^{3+}, Gd^{3+}, Tb^{3+}, and Eu^{3+} ions. Yb^{3+} ions are sensitizers that absorb the excitation light (980 nm) and transfer the energy to the high energy level of Tm^{3+} through energy transfer upconversion (ETU). The Gd^{3+} ions are used to receive energy from Tm^{3+} ions through the energy transfer (ET) approach and pass the energy to Tb^{3+} ions through interfacial energy transfer (IET). After that, part of the energy is released by radiative transitions (Tb^{3+} emission at 545 nm) and the other part is transferred to the Eu^{3+}, leading to its characteristic emission at 615 nm. According to the power-dependent measurements (Fig. S12), the respective emissions of Gd^{3+}, Tm^{3+}, Tb^{3+}, and Eu^{3+} at 311, 345, 545, and 615 nm are all governed by a five-photon process. Fig. S13a and Fig. 2c display the upconversion emission spectra of LNP:x%Tb and LNP:x%

Tb@EuSe nanocomposites ($x = 10, 30, 50, 70, and 100$; $\lambda_{ex} = 980$ nm), respectively. By comparison, the characteristic emissions of Eu^{3+} ions are only observed in the spectra of LNP:x%Tb@EuSe, not in LNP:x%Tb. The 450 and 475 nm emission peaks are ascribed to the $^1D_2 \rightarrow {}^3F_4$ and $^1G_4 \rightarrow {}^3H_6$ electronic transition of Tm^{3+} ions, respectively. The 545 nm emission peak can be attributed to $^5D_4 \rightarrow {}^7F_5$ electronic transition of Tb^{3+} ions and the 615 nm emission peak is derived from $^5D_0 \rightarrow {}^7F_2$ electronic transition of Eu^{3+} ions. It can be observed that the emission intensities of both LNP:x%Tb and LNP:x%Tb@EuSe nanocomposites are changed obviously with different content of Tb^{3+} ions doped. Accordingly, the emission colors of LNP:x%Tb and LNP:x%Tb@EuSe display significant changes as well, owing to the difference of Tb^{3+} content (Fig. 2d and Fig. S13b). These results demonstrate that we achieve the color tuning by changing the relative contribution of Tm, Tb, and Eu upconversion emission in the nanocomposites by modulating the concentration of Tb^{3+} ions in the intermediate layer. The detailed investigation shows that the upconversion emission intensity of Tb^{3+} and Eu^{3+} is closely dependent on the concentration of Tb^{3+} in the interlayer which is in accordance with predictions. This is because under 980 nm excitation, the purposefully designed energy transfer sequence has been implemented, where $Yb^{3+} \rightarrow Tm^{3+}$ upconversion and Gd^{3+} population is followed by energy migration through Gd^{3+} network from the core to the shell dopants, which is then responsible for the population of Tb^{3+} excited states and ultimately feeds Eu^{3+} ions. The emission intensity ratio of Tb^{3+} (545 nm) to Eu^{3+} (615 nm) maximizes with Tb at 30 mol% for the LNP:x%Tb@EuSe (Inset in Fig. 2c). It means that the rates of spontaneous emission and nonradiative energy migration vary with the content of Tb^{3+} ions[46].

To further investigate the nonradiative energy migration and radiative emission in this system, the luminescence decay curves of Tb^{3+} at $^5D_4$ state (monitored at 545 nm) (Fig. 2e) and Eu^{3+} at $^5D_0$ state (monitored at 615 nm) (Fig. 2f) in LNP:x%Tb@EuSe ($x = 10, 30, 50, 70, and 100$) were measured under 980 nm pulse excitation. The results of the corresponding lifetime values were displayed and recorded in Fig. 2g and Table S1. The lifetime at $^5D_4$ state of Tb^{3+} decreases rapidly with the increase of Tb^{3+} concentration, and the lifetime at $^5D_0$ state of Eu^{3+} reaches a maximum at a doping content of 30 mol% of Tb^{3+}. Thus, combined with the spectral results, the following energy transfer model can be deduced: the efficiency of nonradiative energy migration is low, and the energy is mainly used to emit through spontaneous emission for a lower Tb^{3+} content (<30 mol%); the high Tb^{3+} concentration results in a smaller dopant separation that increases the concentration quenching and promotes nonradiative energy migration[47–49]. Moreover, the lifetimes of upconversion emission from

Tb^{3+} and Eu^{3+} (Fig. 2e, f) are much longer than that of Tm^{3+} when the content of Tb^{3+} is low (<30 mol%) (Fig. S14 and Table S1). Similarly, the luminescence lifetime of Tb^{3+} at $^5D_4$ state (monitored at 545 nm) and Tm^{3+} at $^1G_4$ state (monitored at 475 nm) shows the same changing feature in LNP:x%Tb (Fig. S15 and Table S2). In these nanoparticles, the raise of the concentration of Tb^{3+} ions also causes concentration quenching and thus promotes nonradiative relaxation. This characteristic makes it possible to store and decode the information by utilizing time-gating techniques (Fig. S16).

The upconversion luminescence quantum yields of lanthanide-doped nanoparticles are generally very low and less than 1.0 %[50,51]. For the LNP:50%Tb@EuSe nanocomposites, the down-shifting luminescence quantum yield was determined to be 5.226 % when dispersed in cyclohexane by taking rhodamine B as a reference[52,53]. Such quantum yield is sufficient to support the use of nanocomposites for optical anti-counterfeiting. To prove the feasibility of the heterostructured nanocomposite in the optical anti-counterfeiting application, the dual-modal luminescent images based on the upconversion and down-shifting multiplexing were designed. Without further processing, the LNP:50%Tb@EuSe nanocomposites dispersed in cyclohexane were used as the fluorescent ink. As depicted in Fig. 3a, we used a writing brush dipped in fluorescent ink to draw patterns on non-fluorescent paper. The pattern is invisible under natural light, but it is visible when illuminated by specific light sources. The UV light is from a portable UV lamp and the NIR light is from a 980 nm laser equipped with a beam expander. As presented in Fig. 3b, the "SHU" is not visible under natural light, while it emits blue and purple light when irradiated using UV (365 nm) and NIR light (980 nm, 500 mW cm^{-2}), respectively. This demonstrates the potential of the nanocomposites for anti-counterfeiting applications.
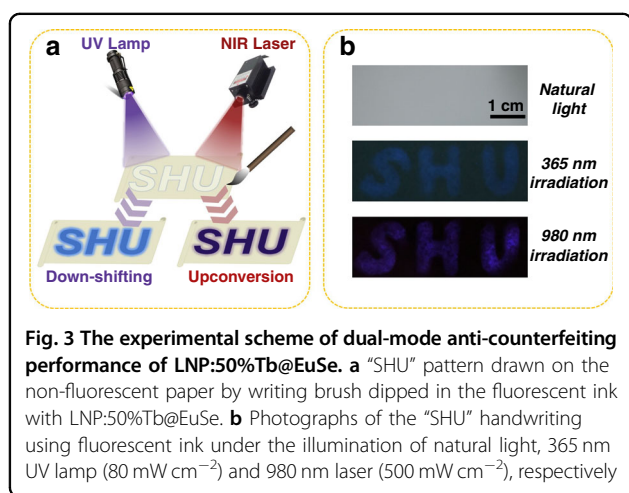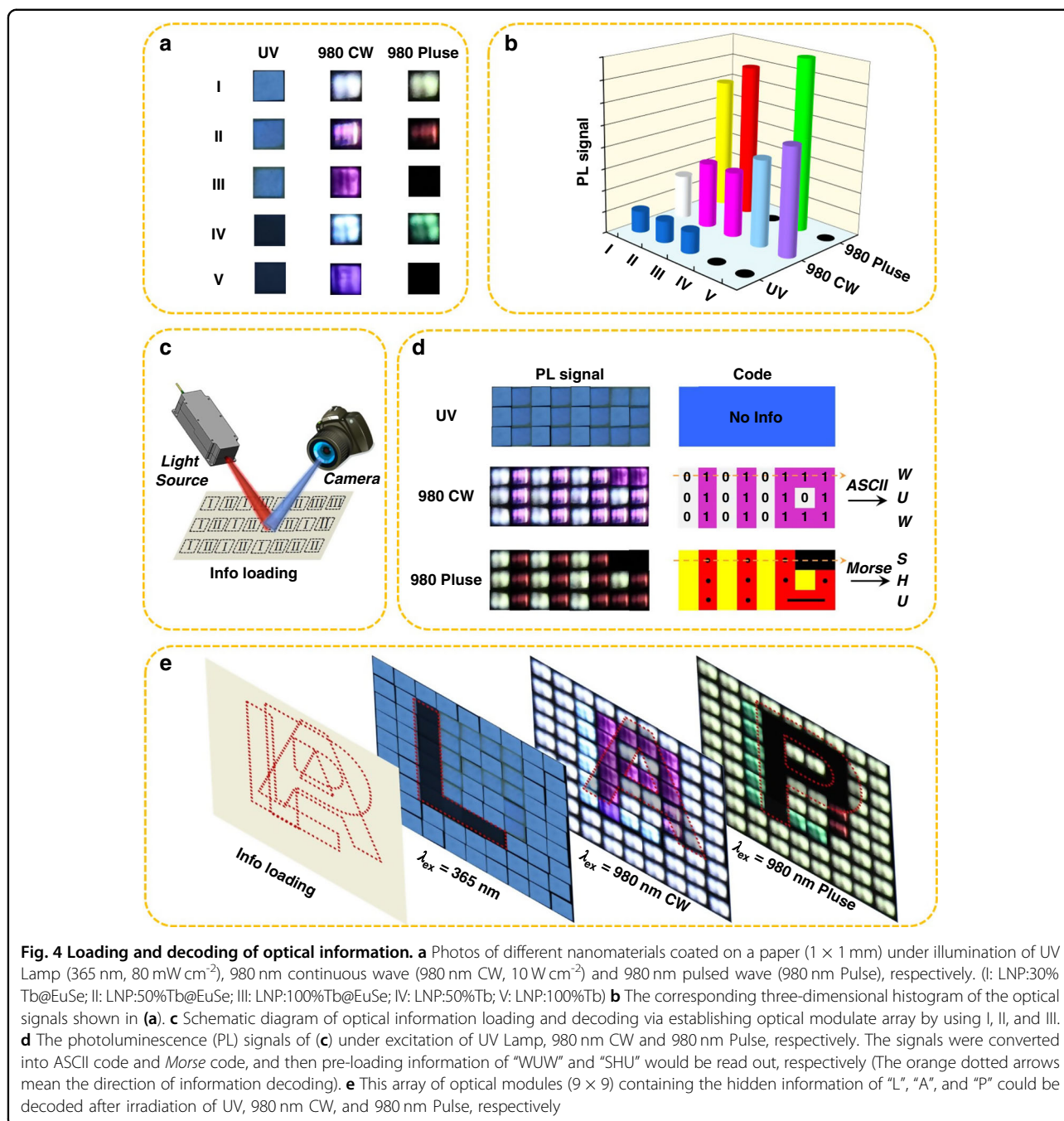

Fig. 3 The experimental scheme of dual-mode anti-counterfeiting performance of LNP:50%Tb@EuSe. a "SHU" pattern drawn on the non-fluorescent paper by writing brush dipped in the fluorescent ink with LNP:50%Tb@EuSe. **b** Photographs of the "SHU" handwriting using fluorescent ink under the illumination of natural light, 365 nm UV lamp (80 mW cm^{-2}) and 980 nm laser (500 mW cm^{-2}), respectively

Encouraged by the good luminescent properties, we selected five different types of the lanthanide-doped nanoparticles and nanocomposites to investigate their suitability for applications in optical information storage. These five kinds of materials dispersed in cyclohexane were used to uniformly paint small (1×1 mm) square markings on non-fluorescent paper (Fig. 4a). They generate eight different visible photoluminescence signals under UV, 980 nm continuous wave (980 nm CW), and 980 nm pulsed laser (980 nm Pulse) excitation, respectively, which is also exhibited as the three-dimensional histogram for the optical signal (Fig. 4b). Every single piece of painted marking coated with luminescence material could be used as a single module with encoded optical information. The different information modules can be assembled in a specific order to store the information and collect the optical signals in different excitation modes. As illustrated in Fig. 4c, three types of optical information modules coated with LNP:x%Tb@EuSe (x = 30, 50, and 100) nanocomposites are manually arranged into a specific array (3 × 8). All the modules emit visible blue light when exposed to the UV light. However, the three types of modules emit different optical signals when the excitation modes were changed to 980 nm CW or 980 nm Pulse (Fig. 4d). On the one hand, the pre-stored information "WUW" could be output via converting the photoluminescence signal into 8-bit ASCII code ($\lambda_{ex} =$ 980 nm CW). On the other hand, "SHU" could be read by converting the luminescence signal into *Morse* code ($\lambda_{ex} =$ 980 nm Pulse). The characteristics of multi-dimensional information load greatly improve the security of information.

The modularity of luminescent materials can greatly increase the capacity of information storage. Not only can we convert photoluminescence signals into codes for advanced information encryption, we also can store the information that we would like to hide via an ordered arrangement of modules under specific excitation mode. As a proof of concept, we created three different modular matrices (9 × 9) and stored the "C", "H", and "N" into different matrices, respectively (Fig. S17). Moreover, we could also store three different messages simultaneously into one array. As shown in Fig. S18 and Fig. 4e, "L", "A", and "P" could be read respectively under the three excitation modes (UV, 980 nm CW, and 980 nm Pulse). At the macroscopic level, we are able to use the multi-mode luminescence of nanocomposites to store different information. In contrast to current popular laser printing multi-dimensional anti-counterfeiting and information storage technologies[54,55], the advantage of the nanocomposites for information storage is that they are more flexible and require less quality of light source. If nanocomposites are loaded in an orderly manner on a substrate using single-particle printing technology, then a 1 ×

Fig. 4 Loading and decoding of optical information. a Photos of different nanomaterials coated on a paper (1 × 1 mm) under illumination of UV Lamp (365 nm, 80 mW cm^{-2}), 980 nm continuous wave (980 nm CW, 10 W cm^{-2}) and 980 nm pulsed wave (980 nm Pulse), respectively. (I: LNP:30% Tb@EuSe; II: LNP:50%Tb@EuSe; III: LNP:100%Tb@EuSe; IV: LNP:50%Tb; V: LNP:100%Tb) **b** The corresponding three-dimensional histogram of the optical signals shown in (**a**). **c** Schematic diagram of optical information loading and decoding via establishing optical modulate array by using I, II, and III. **d** The photoluminescence (PL) signals of (**c**) under excitation of UV Lamp, 980 nm CW and 980 nm Pulse, respectively. The signals were converted into ASCII code and *Morse* code, and then pre-loading information of "WUW" and "SHU" would be read out, respectively (The orange dotted arrows mean the direction of information decoding). **e** This array of optical modules (9 × 9) containing the hidden information of "L", "A", and "P" could be decoded after irradiation of UV, 980 nm CW, and 980 nm Pulse, respectively

1 mm substrate can be loaded with approximately 10^9 nanocomposites, which would be a truly high-capacity optical information storage. Thus, these interesting results further demonstrate that the nanocomposites show excellent potential to store information.

Conclusion

In summary, a series of heterostructured LNP:x% Tb@EuSe nanocomposites were synthesized, in which the cubic EuSe was grown anisotropically on the surface

of hexagonal LNP:x%Tb. The nanocomposites emit blue and white down-shifting emission under 365 nm and 394 nm UV irradiation, respectively. This is due to the fact that the excitation efficiencies of Eu^{2+} and Eu^{3+} are different at different excitation wavelengths and the energy transfer between excited states of Eu^{2+} and Eu^{3+}. Meanwhile, the nanocomposites also show tunable upconversion photoluminescence under NIR laser irradiation (λ_{ex} = 980 nm). In addition, the emission with a longer luminescence lifetime was filtered via the time-

gating technique. Based on the whole feature, the nanocomposites were used for dual-mode anti-counterfeiting and optical information storage. More importantly, a larger information capacity could be achieved when nanomaterials are fabricated into information modules. The results confirm the great potential of the designed LNP:x%Tb@EuSe nanocomposites for advanced anti-counterfeiting and information storage applications. The simple but powerful route provides new perspectives for the development of advanced optical materials and the method of information storage.

Materials and methods
Chemicals and materials

$YCl_3 \cdot 6H_2O$ (99.99%), $GdCl_3 \cdot 6H_2O$ (99.99%), $YbCl_3 \cdot 6H_2O$ (99.99%), $TmCl_3 \cdot 6H_2O$ (99.99%), $TbCl_3 \cdot 6H_2O$ (99.99%), $EuCl_3 \cdot 6H_2O$ (99.9%), Selenium (Se, 99.99%), Tri-n-octylphosphine (TOP, 90%), Oleylamine (OLA, 90%) and methanol (CH_3OH, 99.5%) were acquired from Shanghai Aladdin Biochemical Technology Co. Ltd. Oleic acid (OA, 90%), 1-octadecene (ODE, 90%) and Rhodamine B (analytical standard) were acquired from Sigma-Aldrich Co. Ltd. Ethanol (99.7%), cyclohexane (99.7%), ammonium fluoride (NH_4F, 96%), and Sodium hydroxide (NaOH, 96%) were purchased from Sinopharm Chemical Reagent Co. Ltd. Deionized water is prepared in the lab and used during the whole experiment. All the chemicals were used without further purification.

Synthesis of $NaYF_4$:20%Yb,0.5%Tm core

$NaYF_4$:20%Yb,0.5%Tm core nanoparticles were synthesized and collected according to the previous publication[8].

Synthesis of $NaGdF_4$:Yb,Tm@$NaYF_4$:x%Tb (denoted as LNP:x%Tb)

$NaGdF_4$:Yb,Tm nanoparticles were synthesized based on the previous publication[46]. The system contained $GdCl_3 \cdot 6H_2O$, $YbCl_3 \cdot 6H_2O$, and $TmCl_3 \cdot 6H_2O$ at particular ratio (50:49:1 mol%). $NaGdF_4$:Yb, Tm@$NaYF_4$:x%Tb nanoparticles were synthesized by using the $NaGdF_4$:Yb, Tm nanoparticles as seeds. In detail, ODE (15 mL) and OA (6 mL) were put into a 100 mL flask, then 1 mL water solution containing $YCl_3 \cdot 6H_2O$ and $TbCl_3 \cdot 6H_2O$ at designed ratios were added (Total amount is 0.5 mmol). The mixture was heated to 140 °C for 1 h and then cooled down to 50 °C under vacuum. Subsequently, 0.5 mmol $NaGdF_4$:Yb, Tm nanoparticles along with 10 mL methanol solution containing NaOH (2 mmol) and NH_4F (3 mmol) were added into the flask and stirred for 30 min. The solution was heated to 120 °C under vacuum for 40 minutes and then heated at 300 °C for 1.5 h under an argon flow. The $NaGdF_4$:Yb,Tm@$NaYF_4$:x%Tb nanoparticles were collected and washed as the same as the $NaGdF_4$:Yb, Tm, and dispersed in cyclohexane (5 mL).

Synthesis of LNP:x%Tb@EuSe

Firstly, 0.8 mmol of Se was added to the TOP (800 μL), and Se-TOP was synthesized by ultrasonic treatment for 20 minutes. Subsequently, $EuCl_3 \cdot 6H_2O$ (0.2 mmol), ODE (30 mL), OA (0.3 mL), OLA (3 mL) and pre-synthesized Se-TOP were put into three-necked flask (100 mL). The system was heated to 120 °C under an argon flow for 2.5 h. Then 0.4 mmol LNP:x%Tb were added in the above mixture and the temperate was raised to 290 °C for 3 h. The resulting LNP:x%Tb@EuSe nanocomposites were collected by centrifugation, rinsed with ethanol, and dispersed in 4 mL cyclohexane.

Measurement of quantum yield

The downshifting luminescence quantum yield (φ) of LNP:50%Tb@EuSe nanocomposites dispersed in cyclohexane was determined relative to rhodamine B dissolved in methanol. The quantum yield was calculated using the following equation:

$$\varphi = \varphi_{RB} \times \frac{I_{LNP}}{I_{RB}} \times \frac{E_{RB}}{E_{LNP}} \times \frac{Absorbance(RB)}{Absorbance(LNP)} \times \frac{n_{LNP}^2}{n_{RB}^2}$$

where φ_{RB} is the luminescence quantum yield of rhodamine B, I_{LNP} and I_{RB} stand for integrated luminescence intensity of the LNP:50%Tb@EuSe nanocomposites and rhodamine B (RB), respectively. E is the excitation irradiance, *Absorbance* is the absorbance at the excitation wavelength (the nanocomposites were excited with 365 nm and rhodamine B was excited with 348 nm using the same power density), and n is the refractive index of the corresponding solvent.

Characterization

The emission spectra and luminescence decay curves were recorded by an Edinburgh $FS-5$ fluorescence spectrometer equipped with Xenon lamp and external 980 nm laser [MDL-III-980 nm, cnilaser (Changchun New Industries Optoelectronics Technology Co., Ltd, China)]. The X-ray diffraction (XRD) patterns were collected on 18 KW D/MAX2200 V PC X-ray powder diffractometer. Transmission electron microscopy (TEM) images were collected on JEM-200CX (200 kV). High-resolution transmission electron microscopy (HRTEM), energy-dispersive X-ray spectroscopy (EDS), Scanning transmission electron microscopy and element mapping images were collected on a JEM-2100F (200 kV). X-ray photoelectron spectroscopy (XPS) was measured with an ESCALAB 250Xi. Fourier transform infrared spectroscopy (FT-IR) spectra were recorded by an Avatar 370 in a range of $3500–500 \, cm^{-1}$ with KBr pressed tablets. UV–Vis absorption spectra were recorded by a Shimadzu UV-2600i ultraviolet-visible spectrometer in a range of 300–700 nm. The photos were taken by a digital camera

(Canyon, EOS 5D Mark IV, ISO is 1000 and the acquisition time is 5 ms).

Author details
[1]Department of Physics, College of Sciences, Shanghai University, Shanghai 200444, China. [2]Department of Chemistry, College of Sciences, Shanghai University, Shanghai 200444, China. [3]School of Materials Science and Engineering, Shanghai University, Shanghai 200444, China. [4]Research Center of Nano Science and Technology, College of Sciences, Shanghai University, Shanghai 200444, China. [5]Instrumental Analysis & Research Center, Shanghai University, Shanghai 200444, China. [6]Institute of Low Temperature and Structure Research, Polish Academy of Sciences, 50-422 Wrocław, Poland

Author contributions
All authors have contributed to the results, analysis, discussion, analysis, and manuscript preparation. They have approved the final version of the manuscript.

Conflict of interest
The authors declare no competing interests.

Supplementary information The online version contains supplementary material available at https://doi.org/10.1038/s41377-022-00813-9.

References
1. Gu, M., Li, X. P. & Cao, Y. Y. Optical storage arrays: a perspective for future big data storage. *Light Sci. Appl.* **3**, e177 (2014).
2. Lin, S. S. et al. High-security-level multi-dimensional optical storage medium: nanostructured glass embedded with $LiGa_5O_8$: Mn^{2+} with photostimulated luminescence. *Light Sci. Appl.* **9**, 22 (2020).
3. Zijlstra, P., Chon, J. W. M. & Gu, M. Five-dimensional optical recording mediated by surface plasmons in gold nanorods. *Nature* **459**, 410–413 (2009).
4. Li, Z. W. et al. Creation and reconstruction of thermochromic Au nanorods with surface concavity. *J. Am. Chem. Soc.* **143**, 15791–15799 (2021).
5. Bae, J. et al. 3D-printed quantum dot nanopixels. *ACS Nano* **14**, 10993–11001 (2020).
6. Song, Z. P. et al. Invisible security ink based on water-soluble graphitic carbon nitride quantum dots. *Angew. Chem. Int. Ed.* **55**, 2773–2777 (2016).
7. Huang, X. J. et al. Reversible 3D laser printing of perovskite quantum dots inside a transparent medium. *Nat. Photonics* **14**, 82–88 (2020).
8. Du, K. M. et al. Embellishment of upconversion nanoparticles with ultrasmall perovskite quantum dots for full-color tunable, dual-modal luminescence anticounterfeiting. *Adv. Optical Mater.* **9**, 2100814 (2021).
9. Li, Z. Q. et al. Loading photochromic molecules into a luminescent metal-organic framework for information anticounterfeiting. *Angew. Chem. Int. Ed.* **58**, 18025–18031 (2019).
10. Da Luz, L. L. et al. Inkjet printing of lanthanide-organic frameworks for anti-counterfeiting applications. *ACS Appl. Mater. Interfaces* **7**, 27115–27123 (2015).
11. Ding, W. et al. Multicolour barcoding in one MOF crystal through rational postsynthetic transmetalation. *J. Mater. Chem. C.* **8**, 3176–3182 (2020).
12. Zhang, P. et al. Tuning the photoluminescence of lanthanide metal–organic framework nanospheres through ligand-induced phase transition towards sensing. *J. Mater. Chem. C.* **9**, 6208–6216 (2021).
13. Li, D., Yang, X. G. & Yan, D. P. Cluster-based metal-organic frameworks: modulated singlet-triplet excited states and temperature-responsive phosphorescent switch. *ACS Appl. Mater. Interfaces* **10**, 34377–34384 (2018).
14. Ju, L. et al. A new absorption/fluorescence dual-mode hydrochromic dye for water-jet printing and anti-counterfeiting applications. *J. Mater. Chem. C.* **8**, 2806–2811 (2020).
15. Yang, C. C. et al. Controllable co-assembly of organic micro/nano heterostructures from fluorescent and phosphorescent molecules for dual anti-counterfeiting. *Mater. Horiz.* **6**, 984–989 (2019).
16. Ding, M. Y. et al. Energy manipulation in lanthanide-doped core-shell nanoparticles for tunable dual-mode luminescence toward advanced anti-counterfeiting. *Adv. Mater.* **32**, 2002121 (2020).
17. Li, Z. J. et al. Coloring afterglow nanoparticles for high-contrast time-gating-free multiplex luminescence imaging. *Adv. Mater.* **32**, 2003881 (2020).
18. Wang, Y. K. et al. $NaMgF_3$:Tb^{3+}@$NaMgF_3$ nanoparticles containing deep traps for optical information storage. *Adv. Optical Mater.* **9**, 2100624 (2021).
19. Shikha, S. et al. Versatile design and synthesis of nano-barcodes. *Chem. Soc. Rev.* **46**, 7054–7093 (2017).
20. Ma, B. L. et al. Orthogonal shortwave infrared emission based on rare earth nanoparticles for interference-free logical codes and bio-imaging. *Chem. Sci.* **10**, 3281–3288 (2019).
21. Wu, Y. M. et al. Dynamic upconversion multicolour editing enabled by molecule-assisted opto-electrochemical modulation. *Nat. Commun.* **12**, 2022 (2021).
22. Song, Y. P. et al. Energy migration control of multimodal emissions in an Er^{3+}-Doped nanostructure for information encryption and deep-learning decoding. *Angew. Chem. Int. Ed.* **60**, 23790–23796 (2021).
23. Zhang, H. X. et al. Tm^{3+}-sensitized NIR-II fluorescent nanocrystals for in vivo information storage and decoding. *Angew. Chem. Int. Ed.* **58**, 10153–10157 (2019).
24. Law, L. L. et al. Nonlinear optical activity in dipolar organic-lanthanide complexes. *J. Mater. Chem.* **20**, 4074–4079 (2010).
25. Wang, F. et al. Tuning upconversion through energy migration in core-shell nanoparticles. *Nat. Mater.* **10**, 968–973 (2011).
26. Zhu, X. Y. et al. High-fidelity NIR-II multiplexed lifetime bioimaging with bright double interfaced lanthanide nanoparticles. *Angew. Chem. Int. Ed.* **60**, 23545–23551 (2021).
27. Liu, X. et al. Independent luminescent lifetime and intensity tuning of upconversion nanoparticles by gradient doping for multiplexed encoding. *Angew. Chem. Int. Ed.* **60**, 7041–7045 (2021).
28. Wang, F. et al. Simultaneous phase and size control of upconversion nanocrystals through lanthanide doping. *Nature* **463**, 1061–1065 (2010).
29. Chen, G. Y. et al. Upconversion nanoparticles: design, nanochemistry, and applications in theranostics. *Chem. Rev.* **114**, 5161–5214 (2014).
30. Wen, S. H. et al. Future and challenges for hybrid upconversion nanosystems. *Nat. Photonics* **13**, 828–838 (2019).
31. Auzel, F. Upconversion and anti-stokes processes with f and d Ions in solids. *Chem. Rev.* **104**, 139–173 (2004).
32. Liu, S. B. et al. Tri-channel photon emission of lanthanides in lithium-sublattice core-shell nanostructures for multiple anti-counterfeiting. *Chem. Eng. J.* **397**, 125451 (2020).
33. Liu, X. W. et al. Dual-mode long-lived luminescence of Mn^{2+}-doped nanoparticles for multilevel anticounterfeiting. *ACS Appl. Mater. Interfaces* **11**, 30146–30153 (2019).
34. Liu, Y. S. et al. A strategy to achieve efficient dual-mode luminescence of Eu^{3+} in lanthanides doped multifunctional $NaGdF_4$ nanocrystals. *Adv. Mater.* **22**, 3266–3271 (2010).
35. Wang, C. X. et al. A simple reducing approach using amine to give dual functional EuSe nanocrystals and morphological tuning. *Angew. Chem. Int. Ed.* **50**, 7587–7591 (2011).
36. Zhang, J. Z. et al. Facile synthesis of highly monodisperse EuSe nanocubes with size-dependent optical/magnetic properties and their electrochemiluminescence performance. *Nanoscale* **10**, 13617–13625 (2018).
37. Fischer, S. et al. Bright infrared-to-ultraviolet/visible upconversion in small alkaline earth-based nanoparticles with biocompatible CaF_2 shells. *Angew. Chem. Int. Ed.* **59**, 21603–21612 (2020).
38. Dong, H. et al. Selective cation exchange enabled growth of lanthanide core/shell nanoparticles with dissimilar structure. *J. Am. Chem. Soc.* **139**, 18492–18495 (2017).
39. Ren, Y. F. et al. PEGylated β-$NaGdF_4$/Tb@CaF_2 core/shell nanophosphors for enhanced radioluminescence and folate receptor targeting. *ACS Appl. Nano Mater.* **2**, 3718–3727 (2019).
40. Li, N. et al. High quality ultrathin lanthanide selenide nanostructures with dual modal functionalities. *Chem. Mater.* **28**, 2507–2510 (2016).

41. Zhao, J. X., Chen, B. & Wang, F. Shedding light on the role of misfit strain in controlling core-shell nanocrystals. *Adv. Mater.* **32**, 2004142 (2020).

42. Johnson, N. J. J. & Van Veggel, F. C. J. M. Lanthanide-based heteroepitaxial core-shell nanostructures: compressive *versus* tensile strain asymmetry. *ACS Nano* **8**, 10517–10527 (2014).

43. Pei, P. X. et al. An advanced tunable multimodal luminescent La$_4$GeO$_8$:Eu^{2+}, Er^{3+} phosphor for multicolor anticounterfeiting. *Adv. Funct. Mater.* **31**, 2102479 (2021).

44. Li, K. et al. Recent development in phosphors with different emitting colors *via* energy transfer. *J. Mater. Chem. C.* **4**, 5507–5530 (2016).

45. Zhou, B. et al. Photon upconversion through Tb^{3+}-mediated interfacial energy transfer. *Adv. Mater.* **27**, 6208–6212 (2015).

46. Zhou, B. et al. Probing energy migration through precise control of interfacial energy transfer in nanostructure. *Adv. Mater.* **31**, 1806308 (2019).

47. Boyer, J. C. et al. Synthesis of colloidal upconverting NaYF$_4$ nanocrystals doped with Er^{3+}, Yb^{3+} and Tm^{3+}, Yb^{3+} via thermal decomposition of lanthanide trifluoroacetate precursors. *J. Am. Chem. Soc.* **128**, 7444–7445 (2006).

48. Zhou, B. et al. Controlling upconversion nanocrystals for emerging applications. *Nat. Nanotechnol.* **10**, 924–936 (2015).

49. Haase, M. & Schäfer, H. Upconverting nanoparticles. *Angew. Chem. Int. Ed.* **50**, 5808–5829 (2011).

50. Liu, Q. et al. Sub-10 nm hexagonal lanthanide-doped NaLuF$_4$ upconversion nanocrystals for sensitive bioimaging in vivo. *J. Am. Chem. Soc.* **133**, 17122–17125 (2011).

51. Kaiser, M. et al. Power-dependent upconversion quantum yield of NaYF$_4$:Yb^{3+}, Er^{3+} nano- and micrometer-sized particles - measurements and simulations. *Nanoscale* **9**, 10051–10058 (2017).

52. Wong, K. L., Bünzli, J. C. G. & Tanner, P. A. Quantum yield and brightness. *J. Lumin.* **224**, 117256 (2020).

53. Brouwer, A. M. Standards for photoluminescence quantum yield measurements in solution (IUPAC technical report). *Pure Appl. Chem.* **83**, 2213–2228 (2011).

54. Hu, Z. et al. Reversible 3D optical data storage and information encryption in photo-modulated transparent glass medium. *Light Sci. Appl.* **10**, 140 (2021).

55. Bai, X. et al. Multiple anti-counterfeiting and optical storage of reversible dual-mode luminescence modification in photochromic CaWO$_4$: Yb^{3+}, Er^{3+}, Bi^{3+} phosphor. *Chem. Eng. J.* **429**, 132333 (2022).